J Nanostruct 16(3): 3420-3430, Summer 2026

RESEARCH PAPER

Functionalized Nano-Hydroxyapatite with Chitosan and Glutamic Acid: A Versatile Nano-Adsorbent for Cd(II) Removal from Aqueous Media and a Selective Antifungal Agent

Huda S. Mahdi [1]*, *Saher A. Ali* [1], *Safa H. Ali* [2]

[1] *Department of Chemistry, College of Science, University of Thi-Qar, Al-Nasiriyah, Thi-Qar 64001, Iraq*

[2] *Department of Physics, College of Education, Al-Shatrah University, Al-Shatrah, Thi-Qar 64007, Iraq*

ARTICLE INFO

Article History:
Received 25 March 2026
Accepted 20 May 2026
Published 01 July 2026

Keywords:
Antifungal nanocomposite
Cadmium adsorption
Chitosan
Langmuir isotherm
Nano-hydroxyapatite
Water treatment

ABSTRACT

A nanostructured hydroxyapatite functionalised with chitosan and glutamic acid (n-HAp–Cs–Glu) was prepared via a wet-precipitation route and probed as a dual-purpose material for water remediation and microbial control. Beyond the basic XRD, FTIR, FESEM, TEM and BET data reported earlier, additional characterisation by atomic force microscopy (AFM), energy-dispersive X-ray spectroscopy (EDS) and thermogravimetric analysis was carried out to confirm the nano-scale character and chemical integrity of the composite. The mean crystallite size dropped from 16.65 nm for pristine n-HAp to 12.27 nm after functionalisation, with AFM giving a mean particle diameter near 60 nm. The composite was then tested for Cd(II) uptake from aqueous solutions while varying contact time, dose, pH, initial concentration and temperature. Equilibrium was reached within 75 min and the kinetics were well described by the pseudo-second-order model ($R^2 = 0.9998$), pointing toward a chemisorption-controlled process. Equilibrium data fitted the Langmuir isotherm better than Freundlich, with a maximum capacity of 48.54 mg g^{-1} at 45 °C and separation factors RL well below unity. Thermodynamics were spontaneous ($\Delta G° < 0$), endothermic ($\Delta H° > 0$) and entropy-driven ($\Delta S° > 0$). Antimicrobial assays showed no zone of inhibition against S. aureus or E. coli, but clear activity against the yeasts C. tropicalis and C. albicans, with a maximum inhibition diameter of 8.5 mm at 1000 mg L^{-1}. The findings highlight n-HAp–Cs–Glu as an inexpensive, eco-friendly nano-adsorbent that is also selectively antifungal.

How to cite this article
Mahdi H., Ali S., Ali S. Functionalized Nano-Hydroxyapatite with Chitosan and Glutamic Acid: A Versatile Nano-Adsorbent for Cd(II) Removal from Aqueous Media and a Selective Antifungal Agent. J Nanostruct, 2026; 16(3):3420-3430. DOI: 10.22052/JNS.2026.03.035

INTRODUCTION

Water pollution from heavy metals remains one of the more stubborn problems facing public health, particularly in regions where industrial growth has outpaced wastewater regulation [1–4]. Among the elements typically flagged as hazardous, cadmium (Cd) sits in a difficult position: it is highly toxic even at sub-ppm levels, accumulates in tissues over time and reaches humans through drinking water and the food chain [5–9]. The World Health Organization has set the permissible limit for

* *Corresponding Author Email: hud.mahdi@sci.utq.edu.iq*

Cd(II) in drinking water at 0.005 mg L^{-1}, a value that demands rather efficient removal strategies [10]. Several techniques are commonly used – chemical precipitation, ion exchange, membrane filtration, electrodeposition and adsorption – yet adsorption is generally favoured for being inexpensive, scalable and relatively clean [11,12]. A wide variety of solid sorbents (zeolites, clays, biomass, activated carbon and polymers) have been explored, but capacity and selectivity are often limited [13–17].

Hydroxyapatite, $Ca_{10}(PO_4)_6(OH)_2$, is attractive because of its low solubility, chemical stability and high affinity for di- and trivalent cations [18–19]. Reducing it to the nano-scale further improves its sinterability and reactive surface area [20]. Chitosan, in turn, brings a dense population of –NH_2 and –OH groups that chelate metal ions and disrupt microbial membranes [21–23], while acidic amino acids such as glutamic and aspartic acid alter the crystallinity of HAp through electrostatic and stereochemical effects [24–27]. Combining the three should, in principle, yield a low-crystallinity, highly reactive nano-composite. Building on the n-HAp–Cs–Glu material we previously reported [28], the current work examines its performance as a Cd(II) nano-adsorbent across a range of operational conditions and assesses its antimicrobial behaviour against two bacterial and two fungal isolates.

MATERIALS AND METHODS

Materials

The n-HAp–Cs–Glu nano-composite powder was the same batch we synthesised and partially characterised in our earlier work [29]. Cadmium chloride hemipentahydrate ($CdCl_2{\cdot}2.5H_2O$) was supplied by Hangzhou Hyper Chemicals (China). Hydrochloric acid (35–38 %) was obtained from Alpha Chemika (India) and sodium hydroxide from Fluka. All chemicals were of analytical grade and were used as received. Solutions were prepared with deionised water throughout.

Synthesis of the n-HAp–Cs–Glu nano-composite

The synthesis is summarised in Fig. 1 and is briefly described here for clarity. A $CaCl_2$ solution was first mixed with chitosan (2 %) and the pH adjusted to 10 with NH_4OH. In parallel, glutamic acid (0.2 M, prepared in 1.3 M ammonium acetate) was heated to 80 °C and brought to pH 10. A Na_2HPO_4 solution at the same pH was then

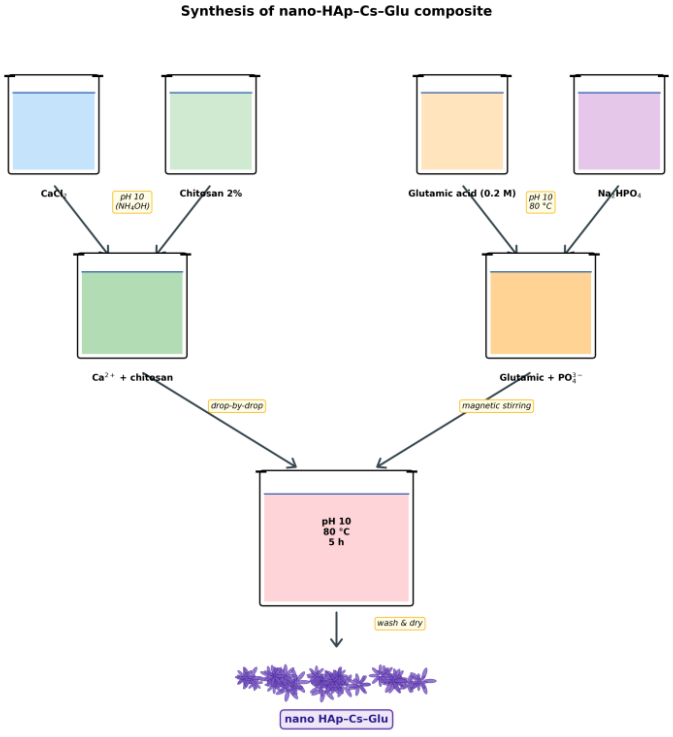

Fig. 1. Schematic of the wet-precipitation route used to obtain n-HAp–Cs–Glu.

added drop-wise to the glutamic mixture under magnetic stirring. The $CaCl_2$/chitosan stream was subsequently introduced drop-wise into the reactor; pH was checked and re-adjusted if needed. Ageing was carried out at 80 °C and pH 10 for 5 h. The white slurry was washed three times with deionised water followed by absolute ethanol, separated by centrifugation, dried at 37°C and kept in a sealed vial. A pristine n-HAp control sample was prepared by repeating the protocol without chitosan or glutamic acid [30].

Additional characterisation

In addition to the techniques reported earlier [31], three complementary methods were applied here. AFM imaging was carried out on a NaioAFM (Nanosurf AG, Switzerland) to obtain 2D and 3D surface views and the mean-diameter distribution of the particles. Elemental composition and elemental mapping were obtained on a Thermo Scientific Axia ChemiSEM diffractometer (EDS). Thermal stability was probed on an HZ2329 TG analyser, with simultaneous TGA, DTG and DSC traces recorded under an air flow at 20 °C min^{-1}.

Adsorption procedure

Stock Cd(II) solutions were prepared by dissolving $CdCl_2 \cdot 2.5H_2O$ in deionised water and

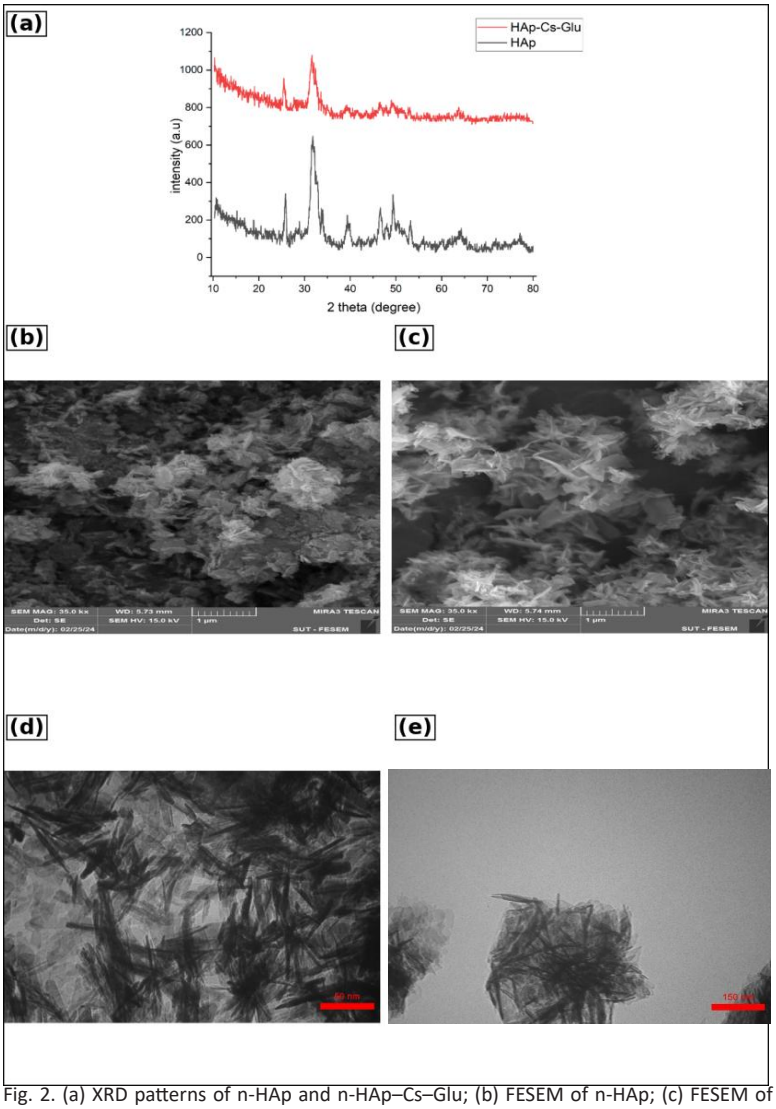

Fig. 2. (a) XRD patterns of n-HAp and n-HAp–Cs–Glu; (b) FESEM of n-HAp; (c) FESEM of n-HAp–Cs–Glu; (d) TEM of n-HAp; (e) TEM of n-HAp–Cs–Glu.

freshly diluted before each run. Batch experiments were performed in 250 mL glass beakers in which 50 mL of the Cd(II) solution was contacted with the n-HAp–Cs–Glu powder under magnetic stirring at 200 rpm. After equilibrium, the suspension was centrifuged at 4000 rpm for 5 min and the residual Cd(II) in the supernatant measured by flame atomic absorption spectroscopy (PG Instruments, Japan; λ = 228.80 nm). The variables tested were the adsorbent dose (0.1–0.2 g), contact time (15–90 min), initial Cd(II) concentration (20–100 mg L^{-1}), pH (3–9; adjusted with 0.1 M HCl or NaOH) and temperature (25–45 °C). Removal efficiency (%) and equilibrium uptake qe (mg g^{-1}) were calculated from Eqs. 1 and 2:

$$R\ \% = (C_o - Ce) \times 100 / C_o \quad (1)$$

$$qe = (C_o - Ce)\ V / m \quad (2)$$

where C_o and Ce are the initial and equilibrium Cd(II) concentrations (mg L^{-1}), V the solution volume (L) and m the mass of adsorbent (g) [32].

Antimicrobial assays

Antibacterial and antifungal screening was performed by the agar well diffusion method on Mueller-Hinton (bacteria) and Sabouraud-dextrose (fungi) agar [33]. Each microbial inoculum was prepared from a single fresh colony suspended in sterile saline. The lawn was spread with a sterile swab and 6 mm wells were punched in the agar. A 100 µL aliquot of n-HAp–Cs–Glu suspension at 250, 500, 750 or 1000 µg mL^{-1} (in DMSO) was loaded into each well. DMSO alone served as the negative control. Bacterial plates were incubated at 37 °C for 18–24 h and fungal plates for 24–48 h. Inhibition-zone diameters were measured in millimetres.

RESULTS AND DISCUSSION

Characterisation of the nano-composite

XRD patterns of n-HAp and n-HAp–Cs–Glu (Fig. 2a) show the characteristic apatite reflections, the most intense at 2θ ≈ 31.7°. After functionalization the peaks broaden and lose intensity, a clear sign of reduced crystallinity. Applying the Scherrer equation to the (211) reflection gave mean crystallite sizes of 21.91 nm for n-HAp and 12.52 nm for n-HAp–Cs–Glu, confirming that chitosan and glutamic acid act as growth-inhibitors during precipitation [34,35]. FESEM micrographs (Fig. 2b

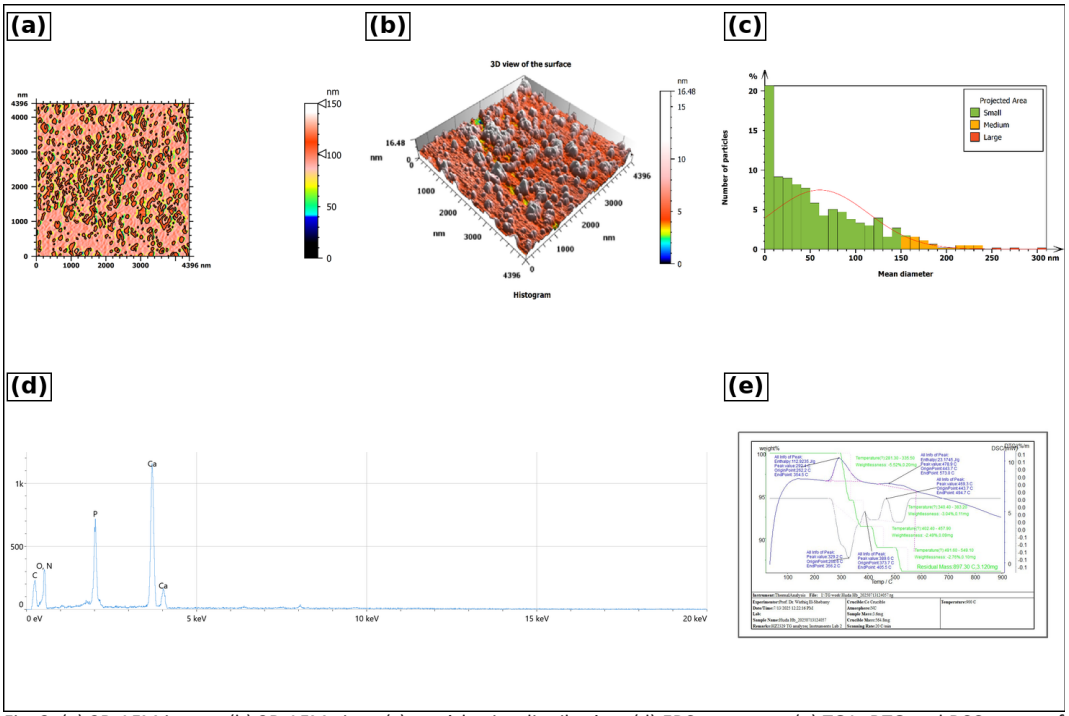

Fig. 3. (a) 2D AFM image; (b) 3D AFM view; (c) particle-size distribution; (d) EDS spectrum; (e) TGA, DTG and DSC traces of n-HAp–Cs–Glu.

and c) show a rough surface with loose aggregates for n-HAp and a clearly more porous, plate-like network for the functionalized composite – useful for adsorption since it raises the available surface area. TEM imaging (Fig. 2d and e) backs this up: the parent n-HAp displays uniform, needle-shaped crystallites whereas n-HAp–Cs–Glu forms flower-like aggregates with a more complex morphology. This kind of morphological evolution is typical when amino acids are present during apatite crystallization [36,37].

AFM imaging supported these observations. The 2D and 3D scans (Fig. 3a and b) revealed a granular, hilly surface with a mean particle diameter of 60.45 nm and a maximum height of 16.48 nm; the size distribution histogram (Fig. 3c) is heavily skewed toward the small-to-medium fraction. EDS analysis (Fig. 3d) detected C, N, O, P and Ca only – an internally clean spectrum without spurious peaks. The corresponding atomic percentages were 28.9 % C, 7.4 % N, 46.5 % O, 5.8 % P and 11.4 % Ca. The Ca/P ratio sat above 1.67, consistent with stoichiometric apatite carrying additional surface-bound Ca^{2+} coordinated by carboxyl and amine groups from glutamic acid and chitosan, in line with prior reports [38]. Thermal analysis (Fig. 3e) showed four mass-loss steps between 280 and 550 °C totalling roughly 14 wt %, with the main DTG/DSC peak near 292 °C corresponding to depolymerization of chitosan and decomposition of the glutamic acid moiety. Above 600 °C the residue was effectively constant, confirming the high thermal stability of the apatite framework [39,40].

Adsorption studies

Effect of contact time and kinetic modelling

Fig. 4a shows that Cd(II) uptake rose sharply during the first 60 min and reached a plateau of 42.93 mg g^{-1} at 75 min; no further change was seen at 90 min, so 75 min was used as the equilibrium contact time in subsequent runs. Such fast initial uptake is expected: a freshly contacted surface has many vacant binding sites, and these saturate as the adsorbed layer grows [41,42].

To probe the underlying kinetics, both pseudo-first-order (Eq. 3) and pseudo-second-order (Eq. 4) models were fitted [43,44]:

$$\ln(qe - qt) = \ln qe - k_1 t \quad (3)$$

$$t / qt = 1/(k_2 qe^2) + (1/qe)\, t \quad (4)$$

The pseudo-first-order plot (Fig. 4b) was clearly poorer (R^2 = 0.84) and yielded a calculated qe of only 15.25 mg g^{-1} – very different from the experimental value, which is itself a strong indication that the model does not apply here. The

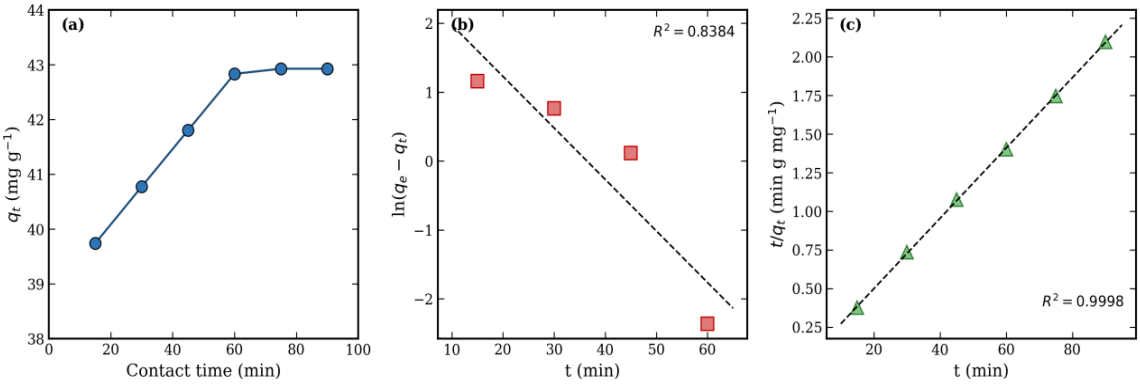

Fig. 4. (a) Effect of contact time on qt; (b) pseudo-first-order plot; (c) pseudo-second-order plot. Conditions: C_o = 100 mg L^{-1}, V = 50 mL, m = 0.1 g, natural pH.

Table 1. Kinetic parameters for Cd(II) adsorption on n-HAp–Cs–Glu.

Model	k	qe (mg g^{-1})	R^2
Pseudo-first-order	0.0748 min^{-1}	15.25	0.8384
Pseudo-second-order	11.9 × 10^{-3} g mg^{-1} min^{-1}	43.86	0.9998

pseudo-second-order plot (Fig. 4c), in contrast, was almost perfectly linear (R^2 = 0.9998), with a calculated qe of 43.86 mg g^{-1} that essentially matches the experimental plateau. Together these results imply that chemisorption – involving the sharing or exchange of electrons between Cd^{2+} and surface functional groups – is the rate-controlling step (Table 1).

Effect of adsorbent dose and pH

Increasing the n-HAp–Cs–Glu mass from 0.1 to 0.2 g raised the Cd(II) removal modestly from 85.9 % to 89.0 %, while the equilibrium uptake fell from 42.9 to 22.3 mg g^{-1} (Fig. 5a). The trend is the usual one: adding more sorbent introduces more binding sites and pushes removal up, but at the same time many of those sites stay unoccupied because the available Cd(II) is fixed, so the per-gram uptake drops [47-45].

The solution pH had a stronger influence (Fig. 5b). At pH 3, qe was only 34.7 mg g^{-1}; raising pH to 9 increased it to 49.0 mg g^{-1}. At low pH, H^+ ions compete with Cd^{2+} for adsorption sites and protonate the chitosan amine groups, both of which weaken Cd(II) binding [48,49]. As pH rises, this competition fades and the surface acquires a net negative character that favours cation uptake [50]. The catch is that at pH > 8, $Cd(OH)_2$ begins to

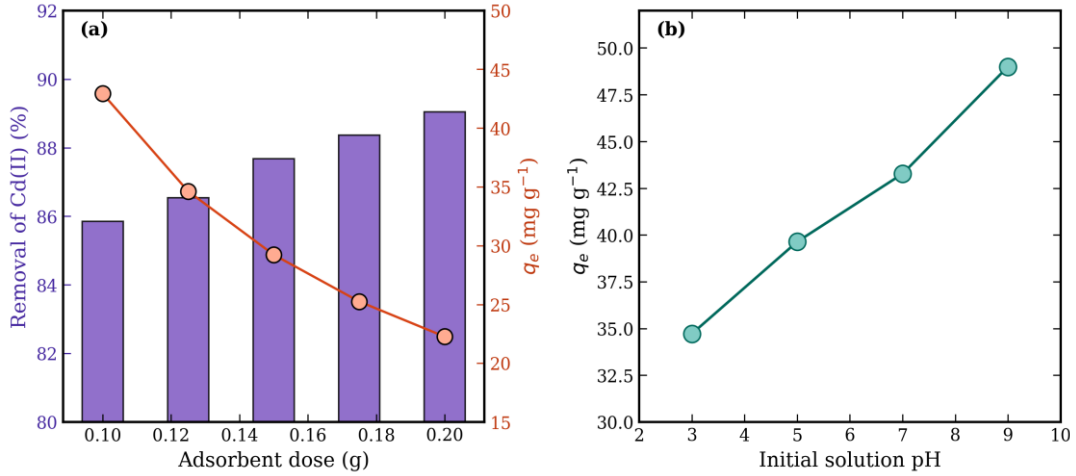

Fig. 5. (a) Effect of adsorbent dose on Cd(II) removal and qe; (b) effect of initial pH on qe. Conditions: C_0 = 100 mg L^{-1}, t = 75 min.

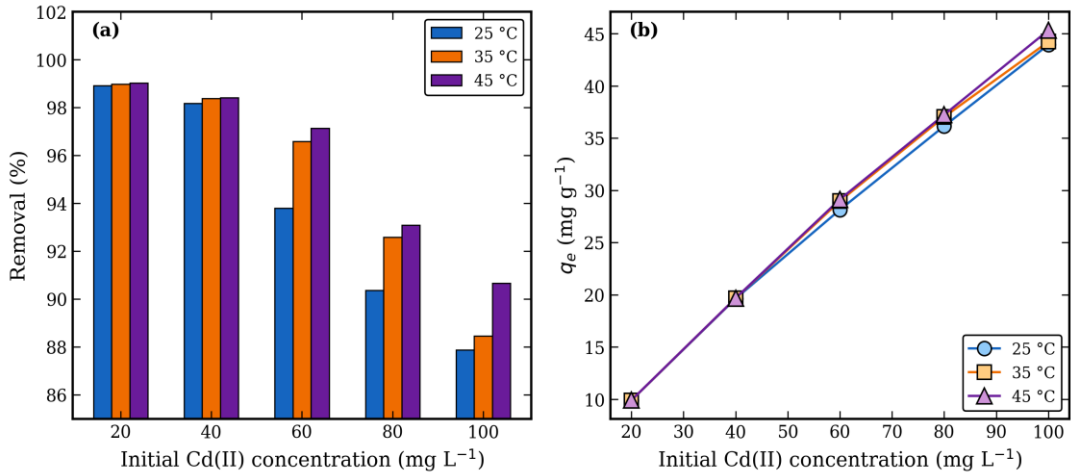

Fig. 6. (a) Cd(II) removal efficiency at three temperatures; (b) equilibrium uptake versus initial concentration at three temperatures.

precipitate, and a fraction of the apparent removal is no longer adsorption. To stay within a regime where adsorption dominates, pH 7 was selected for all subsequent experiments [51].

Effect of initial Cd(II) concentration and temperature

With m = 0.1 g, t = 75 min and pH 7, the Cd(II) concentration was varied between 20 and 100 mg L^{-1} at three temperatures (Fig. 6). At 25 °C the removal efficiency dropped from 98.9 % at 20 mg L^{-1} to 87.9 % at 100 mg L^{-1} (Fig. 6a). At low concentrations there are easily enough vacant sites to capture most of the metal, whereas at high concentrations the fixed amount of sorbent saturates and the residual fraction in solution grows [52]. The opposite trend was seen for qe, which climbed from 9.89 to 43.94 mg g^{-1} (Fig. 6b). A higher driving force across the solution-solid boundary explains this behaviour[53].

Heating the system from 25 to 45 °C lifted both removal efficiency and qe across the entire concentration range. At C_o = 100 mg L^{-1}, qe rose from 43.94 to 45.33 mg g^{-1}, indicating an endothermic process [54,55]. The effect was most pronounced at the highest concentrations, where saturation effects were already starting to bite at 25 °C; warming gave the system enough thermal energy to populate additional, slightly less favourable sites.

Adsorption isotherms

Equilibrium data at 25, 35 and 45 °C were modelled using the Langmuir (Eq. 5) and Freundlich (Eq. 7) equations [56–58,60,61]:

$$Ce/qe = 1/(qm\ kL) + Ce/qm \quad (5)$$

$$RL = 1 / (1 + kL\ C_o) \quad (6)$$

$$\ln qe = (1/n) \ln Ce + \ln KF \quad (7)$$

Fig. 7a and b show the linearised Langmuir and Freundlich plots respectively. Across the three temperatures the Langmuir fit was consistently the better of the two, with R^2 values in the 0.974–0.994 range against 0.959–0.971 for Freundlich (Table 2). qm rose modestly from 46.30 to 48.54 mg g^{-1} between 25 and 45 °C, again pointing to an endothermic interaction. The separation factor RL stayed below 0.04 in all cases (0 < RL < 1), confirming that the adsorption is favourable [56]. The Freundlich exponent n was always between 2.6 and 2.9, also indicating a favourable process [51]; the slight decrease in n with temperature suggests a mild increase in surface heterogeneity, perhaps as previously inaccessible sites become available at higher T.

Fig. 7c presents the van't Hoff plots used to extract the thermodynamic parameters from Eqs. 8–10 [53]:

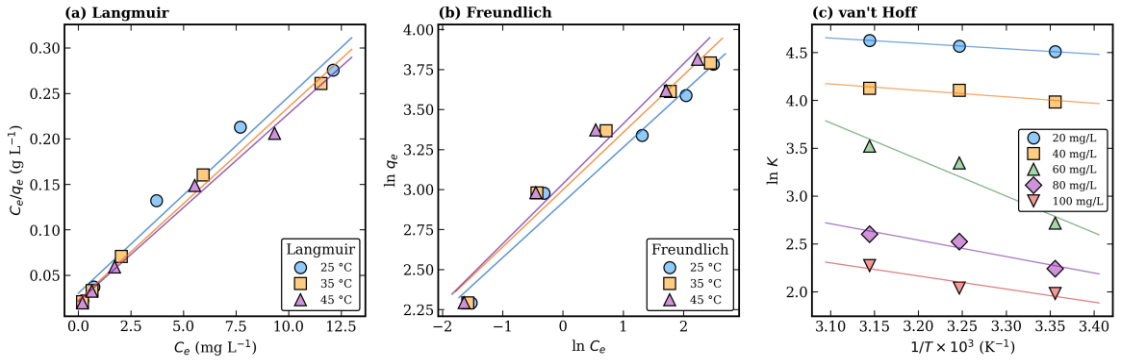

Fig. 7. Linearised isotherm plots: (a) Langmuir; (b) Freundlich; (c) van't Hoff plot for thermodynamic-parameter extraction.

Table 2. Langmuir and Freundlich parameters for Cd(II) adsorption on n-HAp–Cs–Glu.

T (°C)	qm (mg g^{-1})	kL (L mg^{-1})	RL	R^2 (Lang.)	KF	n	R^2 (Freu.)
25	46.30	0.715	0.0306	0.9742	18.52	2.90	0.9708
35	47.17	0.934	0.0236	0.9938	20.04	2.79	0.9586
45	48.54	0.972	0.0228	0.9893	20.81	2.67	0.9629

$$K = CAe / Ce \quad (8)$$

$$\Delta G^\circ = -RT \ln K \quad (9)$$

$$\ln K = -\Delta H^\circ/(RT) + \Delta S^\circ/R \quad (10)$$

Across all initial concentrations and temperatures, ΔG° was negative and grew more negative with T – the adsorption is spontaneous and grows more spontaneous on heating . ΔH° was positive in every case, confirming the endothermic nature suggested by the equilibrium runs, while positive ΔS° values point to increased randomness at the solid–solution interface, possibly because hydration shells around Cd^{2+} are partially shed as the cation binds to the surface [53]. The values for the 60 mg L^{-1} run sit somewhat outside the trend of the other concentrations (ΔH° ≈ 31.8 kJ mol^{-1}), and the corresponding van't Hoff R^2 is lower (0.917). With only three temperature points per concentration, this kind of scatter is not unusual and does not change the qualitative picture, but

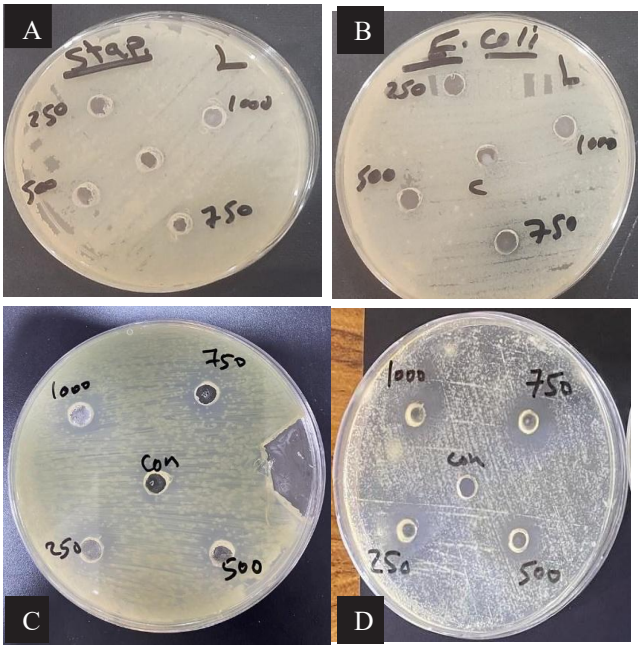

Fig. 8. Agar well-diffusion plates of n-HAp–Cs–Glu against (a) *S. aureus*, (b) *E. coli*, (c) *C. tropicalis* and (d) *C. albicans*. Wells are loaded with 250, 500, 750 and 1000 μg mL^{-1} of the composite.

Table 3. Thermodynamic parameters for Cd(II) adsorption at different initial concentrations.

C_o (mg L^{-1})	ΔH° (kJ mol^{-1})	ΔS° (J mol^{-1} K^{-1})	ΔG° 298 K	ΔG° 308 K	ΔG° 318 K
20	4.64	53.04	−11.17	−11.69	−12.23
40	5.59	52.00	−9.87	−10.51	−10.90
60	31.84	130.00	−6.73	−8.56	−9.31
80	14.27	66.77	−5.55	−6.46	−6.87
100	11.39	54.45	−4.91	−5.22	−6.01

Table 4. Inhibition-zone diameters (mm) of n-HAp–Cs–Glu against the tested microbes.

Microbial isolate	250 μg mL^{-1}	500 μg mL^{-1}	750 μg mL^{-1}	1000 μg mL^{-1}
S. aureus	–	–	–	–
E. coli	–	–	–	–
C. tropicalis	4	–	4	6
C. albicans	8	6	8	8.5

a fourth temperature would be helpful in future work.

Antimicrobial activity

The well-diffusion test produced an interesting and somewhat split picture. At every concentration tested (250–1000 μg mL^{-1}), the n-HAp–Cs–Glu nano-composite gave no measurable inhibition zone against either S. aureus (Gram-positive) or E. coli (Gram-negative); see Fig. 8a and b. The same suspensions, however, did produce clear zones around the wells loaded onto plates inoculated with C. tropicalis and C. albicans (Fig. 8c and d). The largest zone, 8.5 mm, was recorded for C. albicans at 1000 μg mL^{-1}, while C. tropicalis reached 6 mm at the same dose (Table 4).

This selective response is consistent with what has been reported for other chitosan-functionalised inorganic carriers [21,22,62]. Bacterial envelopes – the thick peptidoglycan of Gram-positive cells and the lipopolysaccharide outer membrane of Gram-negative cells – act as steric and electrostatic barriers that limit the penetration of macromolecules. Fungal cell walls, dominated by β-glucan and chitin, are more permissive; the chitosan moiety on the composite surface is also chemically similar to chitin, which probably aids adsorption onto the wall and the subsequent disruption of membrane integrity [63,21]. We note that the dose–response is not strictly monotonic for either yeast (e.g. C. tropicalis gave 4 mm at both 750 and 250 μg mL^{-1}), which suggests that experimental variability between wells and the well-diffusion technique itself contribute meaningfully to the spread; this is a known limitation of the method and a future study using broth microdilution would put more accurate MIC values on these numbers[59,64].

CONCLUSION

A nano-hydroxyapatite functionalised with chitosan and glutamic acid was prepared by wet precipitation and tested for cadmium removal and antimicrobial activity. AFM, EDS and TGA confirmed the nano-scale character (mean particle diameter ≈ 60 nm), the elemental integrity (Ca/P > 1.67) and a thermally robust apatite framework. Cd(II) adsorption fitted the pseudo-second-order kinetic model (R^2 = 0.9998) and the Langmuir isotherm (qm = 48.54 mg g^{-1} at 45 °C), while RL values below unity confirmed favourable uptake. Thermodynamics were spontaneous (ΔG° < 0), endothermic (ΔH° > 0) and entropy-driven (ΔS° > 0). On the biological side, the same nano-composite acted as a selective antifungal agent against C. albicans and C. tropicalis but produced no detec activity against S. aureus or E. coli. Taken together, the results identify n-HAp–Cs–Glu as an inexpensive, environmentally benign nano-adsorbent with a built-in antifungal property – a useful combination for water-treatment applications where biofouling by yeasts is also a concern.

CONFLICT OF INTEREST

The authors declare that there is no conflict of interests regarding the publication of this manuscript.

REFERENCES

1. Arnous MO, Hassan MAA. Heavy metals risk assessment in water and bottom sediments of the eastern part of Lake Manzala, Egypt, based on remote sensing and GIS. Arabian Journal of Geosciences. 2015;8(10):7899-7918.
2. Albaaj ASaa. Analysis and evaluation of sediment pollutants of Euphrates River at Al-Nasiriyah city, south of Iraq. University of Thi-Qar Journal of Science. 2023;10(2):126-130.
3. Khairy S, Afrah Abid M. Estimation of hematological parameters in people exposed to environmental pollution in Thi-Qar Governorate. University of Thi-Qar Journal of Science. 2023;10(2):146-150.
4. Ahmed A, Saher Abdulridha A. Assessment of heavy metals contamination of agricultural soils using pollution indicators in Thi-Qar governorate, Southern Iraq. University of Thi-Qar Journal of Science. 2023;10(2):20-26.
5. Impact of oil waste discharge from Al-Nassiriya oil refinery upon physical chemical properties and heavy elements content of vicinity soil. University of Thi-Qar Journal of Science. 2021:11-15.
6. Hajjabbari S, Fataei E. Determination Cadmium and Lead Pollution Resources of Ardabil Plain Underground Waters. Open Journal of Ecology. 2016;06(09):554-561.
7. Ali SA, Basim YA-K, Haider RA-G. Concentration of some Heavy Elements in Water , Sediment and Plants in Al-Gharraf River in Thi-Qar Province –South of Iraq. University of Thi-Qar Journal of Science. 2020;7(2):69-72.
8. Aufi A. Evalution of Pollution in the Hor AL –Azim Sediments by Heavy metals/ Missan Government / South of Iraq. University of Thi-Qar Journal of Science. 2015;5(2):11-18.
9. Han B. Study on Soil Remediation Technology of Cadmium Contaminated Site. Open Journal of Applied Sciences. 2019;09(03):115-120.
10. Liu B, Wang D, Xu Y, Huang G. Adsorption properties of Cd(II)-imprinted chitosan resin. Journal of Materials Science. 2010;46(5):1535-1541.
11. Chen J, Wang J. Synthesis of Modified Walnut Shell Biochar and Its Performance of Cadmium Adsorption. Journal of Geoscience and Environment Protection. 2023;11(09):317-332.
12. Xu L, Chen J, Wen Y, Li H, Ma J, Fu D. Fast and effective

removal of cadmium ion from water using chitosan encapsulated magnetic Fe3O4 nanoparticles. Desalination and Water Treatment. 2016;57(18):8540-8548.
13. Ji F, Li C, Tang B, Xu J, Lu G, Liu P. Preparation of cellulose acetate/zeolite composite fiber and its adsorption behavior for heavy metal ions in aqueous solution. Chem Eng J. 2012;209:325-333.
14. Celis R, Hermosín MC, Cornejo J. Heavy Metal Adsorption by Functionalized Clays. Environmental Science and Technology. 2000;34(21):4593-4599.
15. Bulgariu D, Bulgariu L. Equilibrium and kinetics studies of heavy metal ions biosorption on green algae waste biomass. Bioresour Technol. 2012;103(1):489-493.
16. Kobya M, Demirbas E, Senturk E, Ince M. Adsorption of heavy metal ions from aqueous solutions by activated carbon prepared from apricot stone. Bioresour Technol. 2005;96(13):1518-1521.
17. Abdel-Halim ES, Al-Deyab SS. Removal of heavy metals from their aqueous solutions through adsorption onto natural polymers. Carbohydr Polym. 2011;84(1):454-458.
18. Aranaz I, Harris R, Heras A. Chitosan Amphiphilic Derivatives. Chemistry and Applications. Curr Org Chem. 2010;14(3):308-330.
19. Elmezayyen AS, Reicha FM. Preparation of Chitosan Copper Complexes: Molecular Dynamic Studies of Chitosan and Chitosan Copper Complexes. Open Journal of Applied Sciences. 2015;05(08):415-427.
20. Kheiri A, Moosawi Jorf SA, Malihipour A, Saremi H, Nikkhah M. Application of chitosan and chitosan nanoparticles for the control of Fusarium head blight of wheat (Fusarium graminearum) in vitro and greenhouse. Int J Biol Macromol. 2016;93:1261-1272.
21. Li R, Zhu L, Liu D, Wang W, Zhang C, Jiao S, et al. High molecular weight chitosan oligosaccharide exhibited antifungal activity by misleading cell wall organization via targeting PHR transglucosidases. Carbohydr Polym. 2022;285:119253.
22. Poznanski P, Hameed A, Orczyk W. Chitosan and Chitosan Nanoparticles: Parameters Enhancing Antifungal Activity. Molecules. 2023;28(7):2996.
23. Suneeta K, Rath P, Sri HKA. Chitosan from shrimp shell (Crangon crangon) and fish scales (Labeorohita): Extraction and characterization. African Journal of Biotechnology. 2016;15(24):1258-1268.
24. Uddin MH, Matsumoto T, Ishihara S, Nakahira A, Okazaki M, Sohmura T. Apatite Containing Aspartic Acid for Selective Protein Loading. J Dent Res. 2010;89(5):488-492.
25. Jahromi MT, Yao G, Cerruti M. The importance of amino acid interactions in the crystallization of hydroxyapatite. Journal of The Royal Society Interface. 2013;10(80):20120906.
26. Gonzalez-McQuire R, Chane-Ching J-Y, Vignaud E, Lebugle A, Mann S. Synthesis and characterization of amino acid-functionalized hydroxyapatite nanorods. J Mater Chem. 2004;14(14):2277.
27. Palazzo B, Walsh D, Iafisco M, Foresti E, Bertinetti L, Martra G, et al. Amino acid synergetic effect on structure, morphology and surface properties of biomimetic apatite nanocrystals. Acta Biomater. 2009;5(4):1241-1252.
28. Smičiklas I, Dimović S, Plećaš I, Mitrić M. Removal of Co2+ from aqueous solutions by hydroxyapatite. Water Res. 2006;40(12):2267-2274.
29. Mobasherpour I, Salahi E, Pazouki M. Removal of nickel (II) from aqueous solutions by using nano-crystalline calcium hydroxyapatite. Journal of Saudi Chemical Society. 2011;15(2):105-112.
30. Ruksudjarit A, Pengpat K, Rujijanagul G, Tunkasiri T. Synthesis and characterization of nanocrystalline hydroxyapatite from natural bovine bone. Current Applied Physics. 2008;8(3-4):270-272.
31. Elouear Z, Bouzid J, Boujelben N, Feki M, Jamoussi F, Montiel A. Heavy metal removal from aqueous solutions by activated phosphate rock. J Hazard Mater. 2008;156(1-3):412-420.
32. Corami A, Mignardi S, Ferrini V. Cadmium removal from single- and multi-metal () solutions by sorption on hydroxyapatite. J Colloid Interface Sci. 2008;317(2):402-408.
33. Mobasherpour I, Salahi E, Pazouki M. Removal of divalent cadmium cations by means of synthetic nano crystallite hydroxyapatite. Desalination. 2011;266(1-3):142-148.
34. Salah TA, Mohammad AM, Hassan MA, El-Anadouli BE. Development of nano-hydroxyapatite/chitosan composite for cadmium ions removal in wastewater treatment. Journal of the Taiwan Institute of Chemical Engineers. 2014;45(4):1571-1577.
35. Akartasse N, Azzaoui K, Mejdoubi E, Elansari LL, Hammouti B, Siaj M, et al. Chitosan-Hydroxyapatite Bio-Based Composite in Film Form: Synthesis and Application in Wastewater. Polymers. 2022;14(20):4265.
36. Huda M, Saher A, Safa A. Synthesis of Hydroxyapatite/Chitosan–Glutamic Acid Nanocomposite for Highly Efficient Removal of Congo Red Dye from Water. Applied Chemical Engineering. 2026.
37. Rahman MS, Sathasivam KV. Heavy Metal Adsorption onto Kappaphycus sp. from Aqueous Solutions: The Use of Error Functions for Validation of Isotherm and Kinetics Models. BioMed Research International. 2015;2015:1-13.
38. Dhanalakshmi CP, Narayanan V, Vijayalakshmi L. Synthesis, characterization and antimicrobial activity of PVA/hydroxyapatite nanocomposites. International Conference on Nanoscience, Engineering and Technology (ICONSET 2011); 2011/11: IEEE; 2011. p. 146-150.
39. Fibryanto E, Amanda H. Characterization of nano-hydroxyapatite–collagen and epigallocatechin-3-gallate (EGCG) composites by scanning electron microscopy-energy dispersive spectroscopy (SEM-EDS), X-ray diffraction (XRD), and Fourier transform infrared (FTIR) spectroscopy. Scientific Dental Journal. 2022;6(2):80.
40. Hamed R, Jodeh S, Hanbali G, Safi Z, Berisha A, Xhaxhiu K, et al. Eco-Friendly Synthesis and Characterization of Double-Crossed Link 3D Graphene Oxide Functionalized With Chitosan for Adsorption of Sulfamethazine From Aqueous Solution: Experimental and DFT Calculations. Frontiers in Environmental Science. 2022;10.
41. Song Y, Wang Q, Yang W, Chen Q, Zhou Y, Zhou L. Chitosan-nickel oxide composite as an efficient adsorbent for removal of Congo red from aqueous solution. J Dispersion Sci Technol. 2021;43(11):1689-1699.
42. Radhi WA, Jasim TE, Jassem AM. Exploring of new Poly(Thiourea-Amide) as a prospective bismarck Brown Y dye adsorbent: Synthesis via ultrasound irradiation, isotherms, kinetic, thermodynamic, and DFT studies. J Indian Chem Soc. 2024;101(10):101329.
43. Mahdi MA, Jawad AAR, Aljeboree AM, Jasim LS, Alkaim AF. Synthesis, Characterization and Adsorption Studies of a Graphene Oxide/Polyacrylic Acid Nanocomposite Hydrogel.

NeuroQuantology. 2021;19(9):46-54.
44. Eddy Jai Poinern G, Krishna Brundavanam R, Thi Le X, Fawcett D. The Mechanical Properties of a Porous Ceramic Derived from a 30 nm Sized Particle Based Powder of Hydroxyapatite for Potential Hard Tissue Engineering Applications. American Journal of Biomedical Engineering. 2013;2(6):278-286.
45. Methylene Blue Dye Removal from Aqueous Solution Using Several Solid Stationary Phases Prepared from Papyrus Plant. Journal of Analytical and Bioanalytical Techniques. 2015.
46. Bhattacharyya KG, Gupta SS. Adsorptive accumulation of Cd(II), Co(II), Cu(II), Pb(II), and Ni(II) from water on montmorillonite: Influence of acid activation. J Colloid Interface Sci. 2007;310(2):411-424.
47. Mohammad AM, Salah Eldin TA, Hassan MA, El-Anadouli BE. Efficient treatment of lead-containing wastewater by hydroxyapatite/chitosan nanostructures. Arabian Journal of Chemistry. 2017;10(5):683-690.
48. Doyurum S, Çelik A. Pb(II) and Cd(II) removal from aqueous solutions by olive cake. J Hazard Mater. 2006;138(1):22-28.
49. Jamshidi Gohari R, Lau WJ, Matsuura T, Halakoo E, Ismail AF. Adsorptive removal of Pb(II) from aqueous solution by novel PES/HMO ultrafiltration mixed matrix membrane. Sep Purif Technol. 2013;120:59-68.
50. Chiou M-S, Li H-Y. Equilibrium and kinetic modeling of adsorption of reactive dye on cross-linked chitosan beads. J Hazard Mater. 2002;93(2):233-248.
51. Wong S, Tumari HH, Ngadi N, Mohamed NB, Hassan O, Mat R, et al. Adsorption of anionic dyes on spent tea leaves modified with polyethyleneimine (PEI-STL). Journal of Cleaner Production. 2019;206:394-406.
52. Bazargan-Lari R, Zafarani HR, Bahrololoom ME, Nemati A. Removal of Cu(II) ions from aqueous solutions by low-cost natural hydroxyapatite/chitosan composite: Equilibrium, kinetic and thermodynamic studies. Journal of the Taiwan Institute of Chemical Engineers. 2014;45(4):1642-1648.
53. Duranoğlu D, Trochimczuk AW, Beker U. Kinetics and thermodynamics of hexavalent chromium adsorption onto activated carbon derived from acrylonitrile-divinylbenzene copolymer. Chem Eng J. 2012;187:193-202.
54. Maleki A, Pajootan E, Hayati B. Ethyl acrylate grafted chitosan for heavy metal removal from wastewater: Equilibrium, kinetic and thermodynamic studies. Journal of the Taiwan Institute of Chemical Engineers. 2015;51:127-134.
55. Liu G, Li Z, Xu L, Xu X, Huang Q, Zeng Y, et al. The dynamics and adsorption of Cd (II) onto hydroxyapatite attapulgite composites from aqueous solution. J Sol-Gel Sci Technol. 2018;87(2):269-284.
56. Kecili R, Hussain CM. Mechanism of Adsorption on Nanomaterials. Nanomaterials in Chromatography: Elsevier; 2018. p. 89-115.
57. Rathi BS, Kumar PS. Application of adsorption process for effective removal of emerging contaminants from water and wastewater. Environ Pollut. 2021;280:116995.
58. Ding L, Zou B, Gao W, Liu Q, Wang Z, Guo Y, et al. Adsorption of Rhodamine-B from aqueous solution using treated rice husk-based activated carbon. Colloids Surf Physicochem Eng Aspects. 2014;446:1-7.
59. Ray SS, Gusain R, Kumar N. Adsorption equilibrium isotherms, kinetics and thermodynamics. Carbon Nanomaterial-Based Adsorbents for Water Purification: Elsevier; 2020. p. 101-118. http://dx.doi.org/10.1016/b978-0-12-821959-1.00005-2
60. Eidan DM, Jasim LS, Al-Suraify SMT, Othman MA-M, Khonakdar HA. Exploring the potential of silver phosphate nanoparticles as a slow-releasing agent to develop antibacterial and biocompatible chitosan-based nanocomposite films. Int J Biol Macromol. 2025;333:148858.
61. Massad Y, Hanbali G, Jodeh S, Hamed O, Bzour M, Dagdag O, et al. The efficiency of removal of organophosphorus malathion pesticide using functionalized multi-walled carbon nanotube: Impact of Dissolved Organic Matter (DOM). Sep Sci Technol. 2021;57(1):1-12.
62. Hanbali G, Jodeh S, Hamed O, Bol R, Khalaf B, Qdemat A, et al. Enhanced Ibuprofen Adsorption and Desorption on Synthesized Functionalized Magnetic Multiwall Carbon Nanotubes from Aqueous Solution. Materials. 2020;13(15):3329.
63. Wu X, Hui KN, Hui KS, Lee SK, Zhou W, Chen R, et al. Adsorption of basic yellow 87 from aqueous solution onto two different mesoporous adsorbents. Chem Eng J. 2012;180:91-98.
64. Ali AA, Tawalbeh M, Al-Othman A. Water Treatment Applications of Green Polymers. Comprehensive Green Materials: Elsevier; 2025. p. 453-469.